

Production and Corrosion Resistance of Thermally Sprayed Fe-Based Amorphous Coatings from Mechanically Milled Feedstock Powders



GUILHERME Y. KOGA, ALBERTO M. JORGE JUNIOR, VIRGINIE ROCHE, RICARDO P. NOGUEIRA, ROBERT SCHULZ, SYLVIO SAVOIE, ANA K. MELLE, CAROLE LOABLE, CLAUDEMIRO BOLFARINI, CLAUDIO S. KIMINAMI, and WALTER J. BOTTA

Mechanically milled FeCrNbB feedstock powders from commercial precursors were used to produce amorphous coatings through two different industrial thermal-spraying techniques: high-velocity oxygen fuel (HVOF) and flame spraying. Microstructure, thermal behavior, and hardness of the coatings and their corrosion resistances in acidic and alkaline chloride-rich media were comparatively studied. HVOF process was effective to produce ~ 200- μm -thick highly amorphous coatings with hardness over than 700 $\text{HV}_{0.3}$ and low porosity (~ 5 pct). Flame-sprayed ~ 220- μm -thick coatings were nanocrystalline, composed of $\alpha\text{-Fe}$, Fe_2B , FeNbB , and Fe_2O_3 phases and presented hardness of 564 $\text{HV}_{0.3}$ and ~ 10 pct porosity. Electrochemical measurements indicated that HVOF coatings exhibit higher corrosion resistance than flame-sprayed ones thanks to the higher amorphous content and lower porosity resulting from the former processing route. Electrochemical impedance spectroscopy results demonstrated that amorphous HVOF $\text{Fe}_{60}\text{Cr}_8\text{Nb}_8\text{B}_{24}$ (at. pct) coatings are interesting to protect mild steels such as the API 5L X80 against corrosion in chloride-rich environments.

<https://doi.org/10.1007/s11661-018-4785-y>

© The Minerals, Metals & Materials Society and ASM International 2018

I. INTRODUCTION

SURFACE corrosion, wear, and fracture are major problems in engineering environments that contribute to the deterioration of structural materials. Fe-based amorphous alloys have been attracting great attention due to their excellent corrosion and wear properties combined with the relatively low cost of iron.^[1–6] However, brittleness greatly restricts their application as structural materials.^[7,8] Coating technology is an

interesting and cost-effective route to overcome the limited plasticity of bulk metallic glasses (BMGs) at room temperature.^[9,10] In addition, the volume restrictions imposed by the critical cooling rates of BMGs are reduced, and therefore, large and complex crystalline substrates can be coated with wear- and corrosion-resistant amorphous alloys.^[10–12]

Fe-based amorphous coatings are an attractive surface technology to protect inexpensive steel components which withstand aggressive environments.^[13–17] However, to obtain thick coatings, amorphous alloys must have a high glass-forming ability (GFA), which is commonly achieved by the addition of an optimal number of noble elements and high purity of raw materials in complex multicomponent systems, hindering their extensive industrial applications. A low-cost and simpler alternative to produce protective amorphous coatings is the Fe-Cr-Nb-B system because (i) it is a system with relatively few components, (ii) it can be obtained from commercial precursors such as trading stainless steel modified with minor low-cost additions (*e.g.*, Fe-B and Fe-Nb),^[18,19] and (iii) it can be designed to present excellent corrosion resistance even with low Cr content (up to 10 at. pct) which does not decrease the GFA.^[20]

GUILHERME Y. KOGA and ALBERTO M. JORGE JUNIOR are with the Departamento de Engenharia de Materiais, Universidade Federal de São Carlos, Rod. Washington Luis, km 235, São Carlos, CEP 13565-905, Brazil and also with the Grenoble Alpes University, CNRS, LEPMI, 38000 Grenoble, France. Contact e-mail: guilherme.koga@dema.ufscar.br VIRGINIE ROCHE and CAROLE LOABLE are with the Grenoble Alpes University, CNRS, LEPMI. RICARDO P. NOGUEIRA is with the Grenoble Alpes University, CNRS, LEPMI and also with the Gas Research Center, Khalifa University of Science and Technology, Abu Dhabi, United Arab Emirates. ROBERT SCHULZ and SYLVIO SAVOIE are with the Hydro-Quebec Research Institute, 1800 Boul. Lionel Boulet, Varennes, QC J3X 1S1, Canada. ANA K. MELLE, CLAUDEMIRO BOLFARINI, CLAUDIO S. KIMINAMI, and WALTER J. BOTTA are with the Departamento de Engenharia de Materiais, Universidade Federal de São Carlos.

Manuscript submitted December 14, 2017.

Article published online July 3, 2018

With respect to the processing route, thermal-spraying techniques have been used to produce amorphous Fe-based coatings thanks to their high deposition rates and the sufficiently rapid cooling rates of molten droplets (10^4 – 10^7 K/s) that inhibit long-range diffusion and crystallization.^[21–23] For instance, Fe-based coatings have been obtained by air plasma spraying (APS),^[24] low-pressure plasma spraying (LPPS),^[25] wire arc spraying,^[26] high-velocity arc spraying,^[27] high-velocity oxygen fuel (HVOF),^[28–30] and flame spraying.^[20,31]

Among the above thermal-spraying techniques, HVOF process is one of the favorite methods to produce dense amorphous Fe-based coatings. Wear- and corrosion-resistant FeCrB amorphous HVOF coatings have been obtained thanks to the high GFA of the alloys together with the proper spraying process parameters, which allow sufficiently high quenching rates upon spraying deposition.^[28–30] The high quality of the resulting HVOF coatings are related to their low-oxidation levels, low-porosity, strong bond adhesion, and large amorphous content, which enhance their wear and corrosion resistances. Similarly, flame spraying has also been used to produce Fe-based protective coatings with a mixture of amorphous and nanostructured microstructure.^[20,31] Although some disadvantages compared to HVOF (*e.g.*, higher porosity, lower bond strength, and low cooling rates), flame spraying demands lower gas consumption and requires a lower cost equipment which reduce the operational costs.^[32]

Amorphous thermally sprayed coatings have been produced from gas-atomized smooth spherical powders.^[33–35] However, due to the restriction of the particle size range, a great fraction of as-atomized particles is often too large to be adequately used as feedstock powders for thermal-spraying techniques. High-energy ball milling is an effective way to reduce the particle size and to homogenize the alloy,^[36] being interesting to adjust inappropriate particles from gas-atomization as feedstock powders to be used in thermal-spraying processes.

In this study, mechanically milled Fe₆₀Cr₈Nb₈B₂₄ (at. pct) feedstock powders obtained from low purity precursors (AISI 430 ferritic stainless steel modified with Fe-Nb and Fe-B) were used to produce amorphous coatings through two different thermal-spraying routes: HVOF and flame spraying. Surfaces were characterized to compare as-sprayed coatings produced from the two different thermal-spraying techniques. Electrochemical measurements were performed in chloride-rich alkaline and acidic media to assess the corrosion-related behavior of the different coatings. Results are shown to be related to the microstructure of the coatings determined by the thermal-spraying route.

II. EXPERIMENTAL PROCEDURE

A. Production of Feedstock Powders and Coatings

Industrial-grade iron-boron (16.5 wt pct B) and iron-niobium (66.5 wt pct Nb) were used to modify a commercial AISI 430 ferritic stainless steel (0.06 wt pct

C, 0.20 wt pct Si, 0.74 wt pct Mn, 17.62 wt pct Cr, 0.37 wt pct Ni, 0.17 wt pct P) to obtain an alloy with a composition close to the Fe₆₀Cr₈Nb₈B₂₄ (at. pct). Feedstock powders were produced through gas-atomization followed by milling in a high-energy ball mill Simoloyer CM08 according to the parameters detailed in Table I. Sieved milled particles (< 53 μm) were selected as feedstock powders for HVOF and flame-spraying processes to coat degreased and sandblasted 120 × 30 × 5 mm API 5L X80 steel substrates (0.07 wt pct C, 0.21 wt pct Si, 1.64 wt pct Mn, 0.10 wt pct Cr, 0.25 wt pct Ni). The ensemble of the spraying parameters is summarized in Table II.

B. Characterization of Powders and Coatings

Morphology and chemical composition of the gas-atomized and milled feedstock powders were characterized by scanning electron microscopy (SEM) coupled to a wavelength-dispersive X-ray spectroscopy (WDS). Phase constituents were identified by X-ray diffraction (XRD) analysis performed on an X-ray diffractometer Rigaku Geigerflex ME210GF2, with Cu-K α radiation. The thermal stability was examined by differential scanning calorimetry (DSC), in a Netzsch 404, at the heating rate of 0.67 K/s.

The microstructure and structure of coatings were examined by scanning electron microscopy (SEM), in a Philips XL30 FEG equipped with energy-dispersive spectroscopy (EDS) (OXFORD-LINK ISIS 300), transmission electron microscopy (TEM) in a Philips (FEI) CM 120 operated at 120 kV, and X-ray diffraction (XRD) analysis as described above. Cross-sectional samples were mounted in conducting resin. After grinding and polishing, they were examined in the SEM using backscattered electron and secondary electron signals to form images. Thin coating slices for TEM were first peeled from substrates and grounded to about 50 μm thickness, and then thinned by ion milling technique until perforation in a GATAN PIPS, using low energy.

Detached coatings used in TEM and thermal analyses were obtained as follows: first, the coated substrate was held against a grinding wheel, scraping the substrate up to near the deposit interface. Then, the specimen was bent as sharply as possible first to one side then to the other to break the sample. This procedure generates a shearing stress between the remaining base metal and the deposit, causing part of the deposit to separate from the substrate. Finally, the peeled sample was obtained by using a sharp chisel at the back of the coating overhang.

Thermal behavior of detached coatings was investigated using the above-described DSC. The average level of coatings' porosity was evaluated through image analysis of cross-sectional microstructures using the software AnalySIS Pro. A total of 20 cross-sectional images were taken in different regions of coatings using a CARL ZEISS optical microscope (magnification of 500 times). The carbon contents of the feedstock powder and of the detached thermally sprayed coatings were

Table I. Gas-Spraying and High-Energy Milling Parameters of Feedstock Powder Production

Gas-Atomization		High-Energy Ball Milling	
Atmosphere during melting	argon	atmosphere during milling	argon
Atomization gas	N ₂	ball-to-powder ratio	10:1
Gas flow rate—N ₂ (m ³ /min)	5.9	ball diameter (mm)	5
Mass flow rate (kg/min)	0.62	milling rotation speed (rpm)	650
Casting temperature (°C)	1700	milling time (h)	12
Nozzle diameter (mm)	6.0	discharging rotation speed (rpm)	300
		discharging time (h)	5

Table II. Spraying Parameters Employed in the HVOF and Flame-Spraying Processes

HVOF Process		Flame-Spraying Process	
Torch model	TAFA model 5220	torch model	TeroDyn 2000 torch
Torch manufacturer	praxair surface technology	torch manufacturer	Castolin Eutetic
Spraying equipment	TAFA JP-8000	spraying equipment	TeroDyn 2000
Standoff distance (mm)	300	standoff distance (mm)	100
Oxygen (MPa)	8.96×10^5	oxygen (MPa)	4.96×10^5
Kerosene (MPa)	6.96×10^5	acetylene (MPa)	2.41×10^5
Carrier gas	argon	carrier gas	—
*Coating thickness (μm)	195 ± 7	*coating thickness (μm)	222 ± 17

*Thickness presented as the mean value and the standard deviation based on 10 measurements using cross-sectional SEM images.

determined by a LECO CS-444 equipment, the analysis being repeated one more time to ensure the repeatability.

Vickers hardness measurements in different cross-sectional regions were performed on coatings using a Vickers diamond indenter (Newage Testing Instrument, model Auto-C.A.M.S. Computer-Assisted Microhardness System) applying a load of 300 g with a dwell time of 15 seconds. An average value was obtained from at least ten individual measurements in each specimen. The size of the Vickers hardness indentations was large enough to cover several different phases of the coatings. Therefore, the reported values represent the overall hardness of the coating.

C. Corrosion Measurements

Polarization curves and electrochemical impedance spectroscopy (EIS) tests were carried out by a conventional three-electrode cell setup at room temperature and open to air. The working electrodes (WE) were 1 cm² polished specimens of the different coatings (flame spraying and HVOF) as well as a bare API 5L X80 steel substrate one to which the prepared coatings have been compared to. The counter electrode was a platinum (Pt) sheet, and a saturated calomel electrode (SCE) was used as the reference electrode. Electrochemical measurements were performed in acidic (pH = 3) and alkaline (pH = 10) chloride-rich (3.5 wt pct NaCl) solutions to evaluate the corrosion resistance. All the solutions were prepared with deionized water and additions of H₂SO₄ and NaOH to adjust the pH of acidic and alkaline electrolytes, respectively. Measurements were launched after 30 minutes of immersion of the sample in the

solution to allow steady free potential conditions to be reached. Potentiodynamic polarizations were obtained using a scan rate of 1 mV/s and EIS at the corrosion potential in a frequency range between 50 kHz to 10 mHz. Reproducibility of data was ensured by repeating the test two times.

III. RESULTS AND DISCUSSION

A. Characterization of Powders and Coatings

Ranges of particle size distribution and micrographs of gas-atomized powders are presented in Figure 1. Broad particle size distribution is a characteristic of gas-atomized powders where small particles exhibit smooth (near) spherical shape, while large particles present plate-like shape. These different morphologies are related to the differences in cooling rates which are higher for smaller particles.

As stated in the introduction, the interest is to use the gas-atomized large plate-like particles, Figure 2(a), as feedstock powders after high-energy milling, Figure 2(b). Although milled powders show irregular shapes due to the repeated fracture during high-energy milling of gas-atomized particles, their morphologies are much smoother than the precursor large plate-like gas-atomized ones. WDS chemical analyses performed on several different feedstock particles, Table III, indicate that the chemical composition of milled feedstock powders is consistent with the nominal Fe₆₀Cr₈Nb₈B₂₄ alloy, despite the presence of some impurities from the low-purity raw materials and further contamination during the milling.

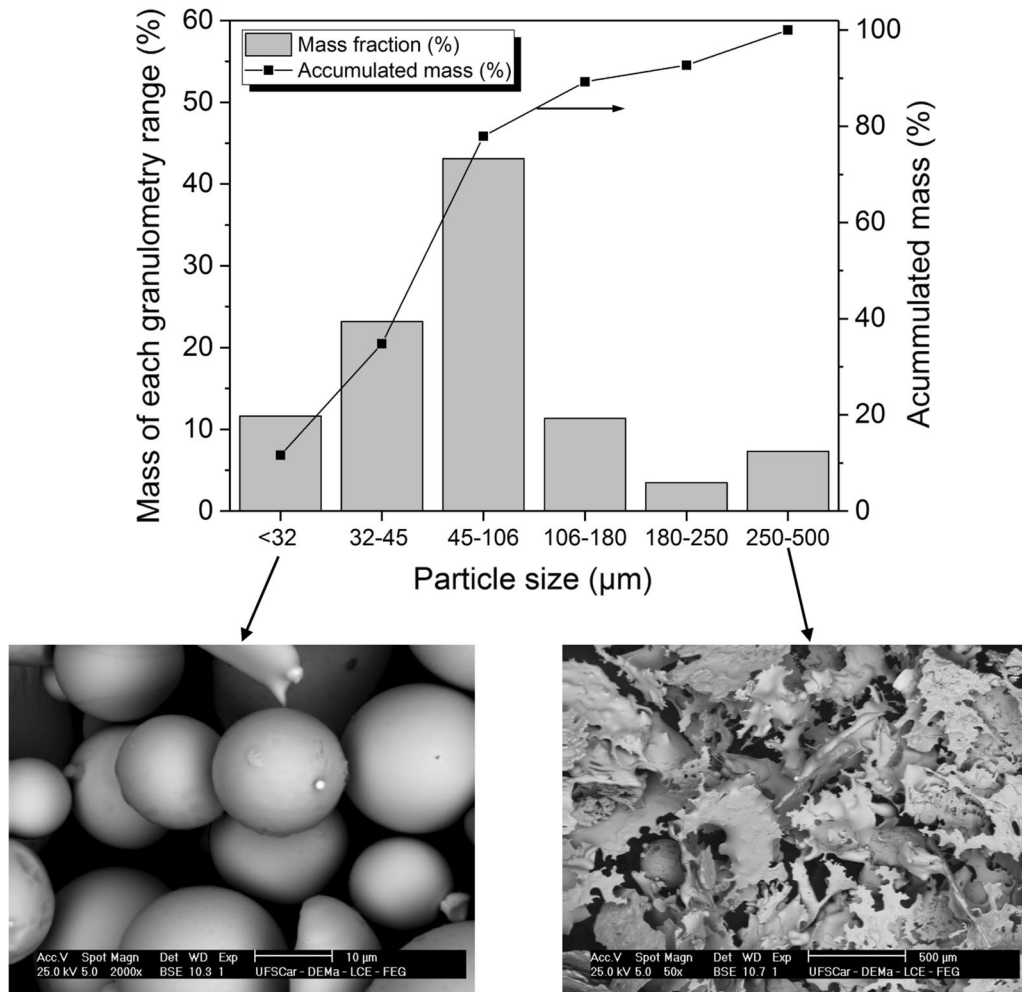


Fig. 1—Particle size distribution of the gas-atomized powders which highlights different morphologies varying from near-spherical (small particles) to plate-like (large particles) shapes.

Thermal-spraying processes such as HVOF and flame spraying may introduce carbon to the particles upon spraying deposition. The carbon content average, from two measurements, of the feedstock powder was 0.17 wt pct, and those of the HVOF and flame-sprayed coatings were 0.21 and 0.32 wt pct, respectively. The increment of the carbon content on the coatings due to thermal-spraying processes could represent a potential concern regarding the stability of the amorphous alloy. However, the addition of small atoms such as carbon and boron has normally a positive effect on the amorphization of Fe-based alloys—the reason why different Fe-B-C-based alloys with high GFA have been developed.^[37–39] Indeed, it has been reported that carbon contaminations as high as 10 at. pct do not have any detrimental effect on the GFA of some mechanically milled Fe-based alloys and can even improve their GFA.^[40] Also, Fe-B-C-based cast alloys with high GFA, with carbon content as high as 15 at. pct, are reported.^[41] In other words, the inherent risk of contamination of the chosen processing route, HVOF and flame spraying, is related to the carbon incorporation which is unlikely to decrease the GFA of the alloy under interest.

Figure 3 shows the microstructure of as-sprayed coatings produced by flame-spraying and HVOF processes. Flame-sprayed coatings, Figure 3(a), are composed of well-flattened splats and partially or unmolten particles which appear as several protrusions on the as-sprayed surface, Figure 3(b). Similar to the flame-sprayed coatings, the HVOF ones are mainly composed of well-flattened and adherent lamellae morphology, however, with fewer partially or unmolten particles, suggesting higher compaction during the deposition as verified in Figure 3(c). Moreover, the HVOF as-sprayed surface is mainly composed of featureless areas, corresponding to molten feedstock powders which splashed against the substrate, as seen in Figure 3(d).

Flame-spraying technique has inherent disadvantages compared with the HVOF process, such as lower spraying velocity. Because of the different processing routes, HVOF coatings present higher lamellae adhesion, lower porosity (~ 5 pct), and higher Vickers hardness ($735 \pm 25 \text{ HV}_{0.3}$) compared with the flame-sprayed coatings (~ 10 pct of porosity and $564 \pm 15 \text{ HV}_{0.3}$). This is mostly due to the higher kinetic energy of molten droplets in the case of HVOF

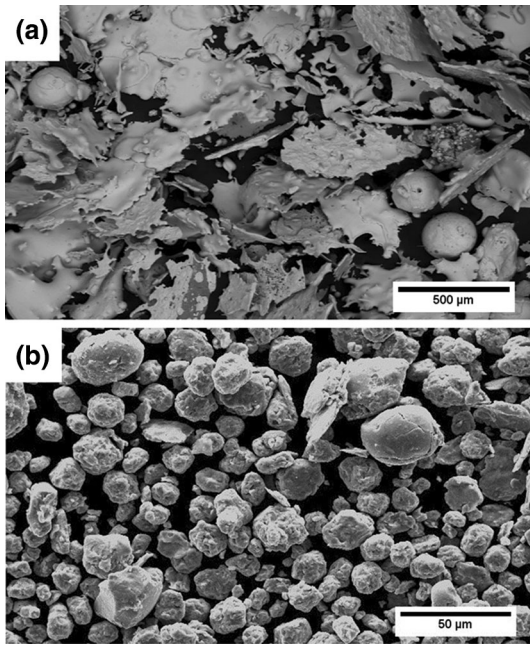


Fig. 2—Secondary electron SEM images of (a) large gas-atomized particles, particle sizes ranging between 53 and 500 μm ; and (b) resulting feedstock powders with size inferior to 53 μm from the high-energy milling of gas-atomized particles between 53 to 500 μm .

and the larger fractions of semimolten and solid particles during the flame-spraying deposition.

The amorphous content of the resulting thermally sprayed coatings depends on the spray parameters as well as on the alloy composition. Figures 4(a) and (b) show the XRD patterns and the DSC curves of powders and coatings, respectively. XRD results of gas-atomized particles and milled feedstock powders exhibit a broad halo single peak, which indicates high amorphous phase content, which may be attributed to the good GFA of the $\text{Fe}_{60}\text{Cr}_8\text{Nb}_8\text{B}_{24}$ (at. pct) alloy. The emergence of a single broad diffraction halo superimposed by a small Bragg peak ($2\theta = 45^\circ$) is associated with the formation of a crystalline phase, indicating that the HVOF coatings are essentially amorphous. Flame-sprayed coatings exhibit a broad diffraction halo at about $2\theta = 45^\circ$ together with several broad diffraction peaks. This indicates the presence of a small amount of an amorphous phase and plenty of nanocrystals, which were indexed to be the $\alpha\text{-Fe}$, Fe_2B , FeNbB , and Fe_2O_3 crystalline phases. The flame-spraying coatings exhibited an oxygen-rich phase, Fe_2O_3 according to the microanalysis in the selected locations of dark regions in Figure 3(a), while the HVOF coatings did not. This is because the higher cooling rates experienced by the particles during HVOF deposition suppressed the formation of oxides and the oxygen remained in solid

Table III. Theoretical and Measured Compositions of the Milled Feedstock Powders

Chemical composition at. pct	Fe	Cr	Nb	B	Impurities
Theoretical alloy	60	8	8	24	—
Real composition ^a	67 ± 6	8.0 ± 0.7	6 ± 1	17 ± 6	bal.

^aAverages and standard deviations calculated from WDS measurements taken in several different particles.

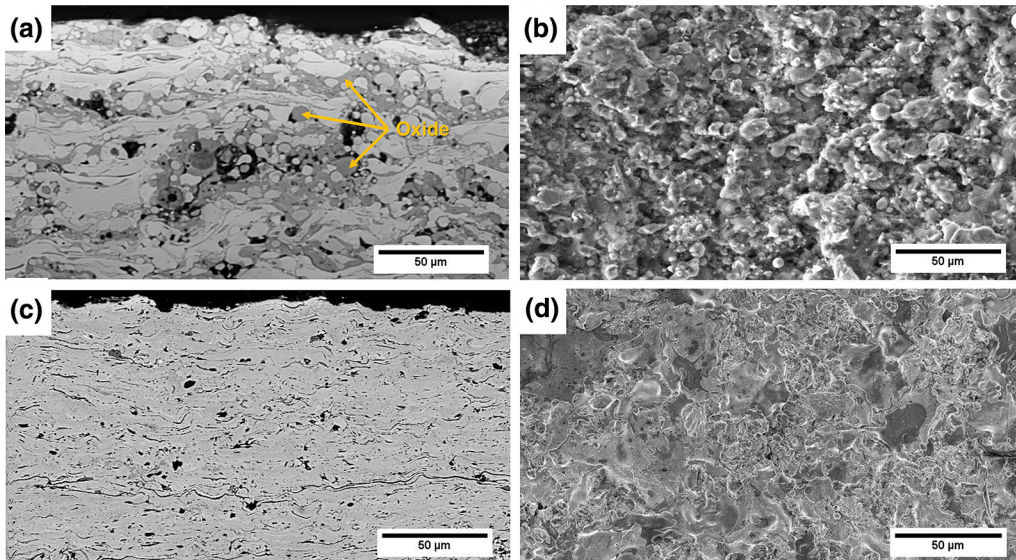


Fig. 3—Backscattered electron images (500 times) of the cross-sectional region of (a) flame-sprayed coating and (c) HVOF coating. Secondary electron micrograph (500 times) of the as-sprayed top surface of (b) flame-sprayed coating and (d) HVOF coating.

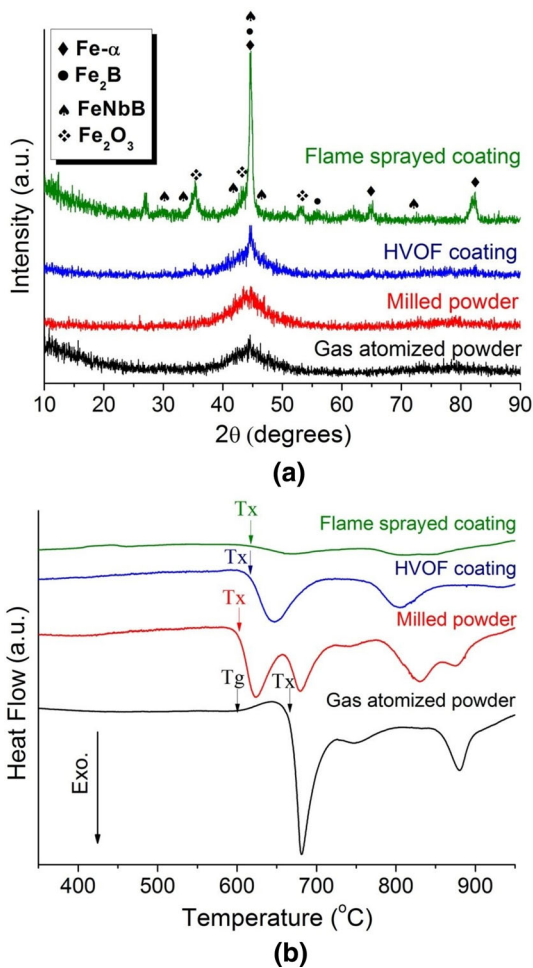


Fig. 4—(a) XRD and (b) DSC curves of the gas-atomized particles, feedstock milled powders, and thermally sprayed coatings produced by HVOF and flame-spraying processes.

solution within the amorphous matrix. Moreover, oxidation of particles upon HVOF deposition is generally lower than that during flame spraying due to the shorter residence time in the zone of combustion.

DSC curves presented in Figure 4(b) indicate different thermal behaviors of gas-atomized and milled powders. Gas-atomized powders exhibit glass transition temperature (T_g) and a large supercooled liquid region ($\Delta T_x = T_x - T_g = 63$ K), suggesting high thermal stability of the supercooled liquid against crystallization. However, high-energy milling affected the crystallization, as shown by the changes in the DSC curves. High-energy milling introduces internal stresses that selectively increase the temperature, locally reducing the free volume, which may promote different crystallization behaviors and even clustering modifications,^[36,42,43] in this last case producing an amorphous structure different from that of the precursor amorphous material. In addition, a decrease in the crystallization temperature and a depression of crystallization activation energies compared to the as-solidified amorphous alloys have been reported.^[44–46]

Reinforcing the above comments, Figure 4(b) clearly indicates that milled and atomized powders are

structurally different. In addition to the differences in their crystallization temperatures, one can observe the absence of T_g and the splitting of first and second crystallization peaks for milled particles. However, crystallization enthalpies were similar for atomized and milled powders, confirming that even milled ones are fully amorphous as presented in Figure 4(a).

From the above discussion, one could say that thermally sprayed coatings are more stable than feedstock powders because T_x has increased a bit. Comparing both kinds of coatings, one will observe that the amorphous states for HVOF and flame-sprayed samples are structurally similar because they have the same T_x and crystallization peak temperatures. Apparently, the thermal cycle returned the original structure present in the atomized powders as suggested by the shapes of the DSC curves for either HVOF or flame processing compared to the shape of the DSC curve of the as-atomized powders. However, the DSC curves of the HVOF and flame coatings show an early crystallization and crystallization peaks in temperatures smaller than for as-atomized powders.

Indeed, the amorphous state of both HVOF and flame-sprayed samples are clearly less stable than atomized powders, although being more stable than milled ones. This phenomenon implies that, despite crystallization, after thermal cycling, the amorphous state of the final coating will be more stable at higher temperatures than milled powders. Furthermore, the huge differences in enthalpies confirm almost full crystallization of flame-sprayed coatings when compared to HVOF ones (Figure 4(b)). HVOF process allows higher cooling rates, up to 10^7 K/s,^[47] than flame spraying, $\sim 10^4$ K/s, enabling the formation of a higher fraction of amorphous phase. An increase of the cooling rates up to 10^6 K/s during flame-spraying deposition can be achieved but a special water-cooled copper substrate is required.^[48]

TEM analysis was undertaken to obtain more detailed information about the microstructure of the coatings. Despite the variation in size and thermal history of each particle and the resulting splats during the thermal-spraying process, important features can be observed in Figure 5. Coatings obtained through HVOF and flame spraying present nanocrystals embedded within an amorphous matrix. However, the coating obtained by flame spraying displays larger volume fraction of nanocrystals, Figure 5(b), than in sample obtained by HVOF, Figure 5(a). The diffraction pattern from HVOF coating (inset of Figure 5(a)) shows a large diffuse halo with scattered diffraction spots arising from crystalline grains within the selected area which indicate a substantial fraction of an amorphous phase and some embedded nanocrystalline particles, indexation of which can be inferred from Figure 4(a). Conversely, the electron diffraction pattern displayed in the inset of Figure 5(b) for the flame-sprayed coatings presents a thinner amorphous halo superimposed by a large number of spots indicating a rather large fraction of nanocrystals, indexation of which can also be inferred from Figure 4(a), and a smaller amount of amorphous phase.

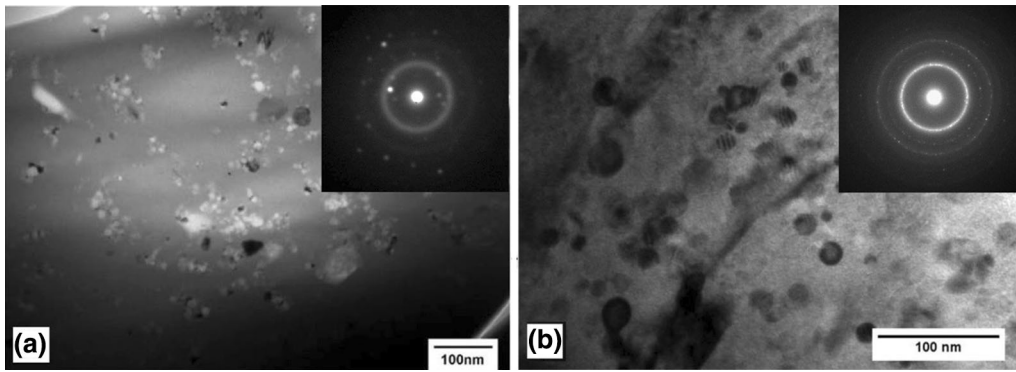


Fig. 5—Brightfield TEM micrographs indicating the differences of the crystalline phases and matrices of the coating produced by (a) HVOF and (b) flame spraying. Insets represent selected area electron diffraction pattern (SAEDP).

B. Corrosion Behavior of API 5L X80 Steel and Thermally Sprayed Coatings

Samples were evaluated in both acidic and alkaline chloride-rich media with results following a similar general trend of better performance of the HVOF coatings in both conditions. This general behavior is illustrated in Figure 6 that shows polarization curves of thermally sprayed coatings and API 5L X80 steel in chloride-rich acidic media. HVOF coatings present nobler corrosion potential (E_{corr}) and lower corrosion current density (i_{corr}) compared to flame-sprayed coatings and API 5L X80 steel. In addition, HVOF coatings present a broad current density plateau upon anodic polarization instead of exhibiting a monotonic increase in current density as for both the flame-sprayed coatings and API 5L X80 steel. Table IV summarizes i_{corr} and E_{corr} values obtained from the cathodic polarization curves in acidic and alkaline chloride-rich media which exhibit better Tafel's behavior, especially for the passivated HVOF coatings. The API 5L X80 steel exhibits poor corrosion resistance either in alkaline or acidic chloride-rich solutions. Thermally sprayed coatings present similar E_{corr} , but HVOF specimens show lower values for i_{corr} than the ones for flame-sprayed samples. General trends indicate that either in acidic or alkaline chloride-rich media, HVOF coatings are more effective to protect the API 5L X80 steel against corrosion.

In a first approach, the clearly better corrosion-resistance performance of HVOF coatings regardless of the pH can be ascribed to their higher amorphous content (Figures 4 and 5) as well as their low porosity (~ 5 pct), which assure low i_{corr} compared to flame-sprayed coatings. In general, if one considers the same composition, high porosity^[49,50] and crystallization^[51–53] greatly impair the corrosion resistance of amorphous metallic coatings. Porosity defect may impact the corrosion resistances of Fe-based amorphous coatings because preferential channels for corrosive chloride-rich electrolyte movement toward the coating-substrate interface can be formed. Pores also represent potential occluded regions for pitting or crevice initiation. Globally, porosity reduces the corrosion resistance of thermally sprayed Fe-amorphous coatings, increases the passive current density, and lowers the stability of the

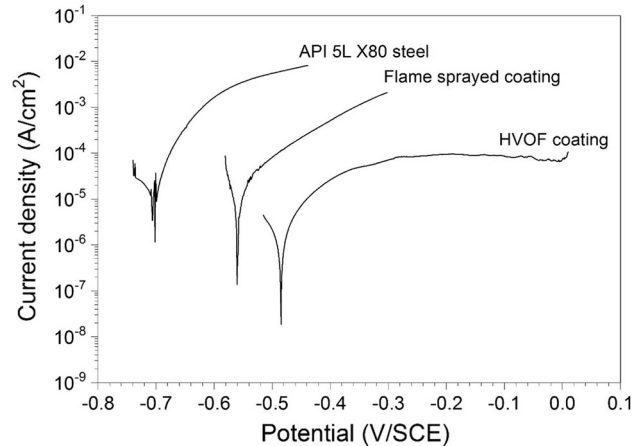


Fig. 6—Potentiodynamic polarization curves of thermally sprayed coatings and API 5L X80 steel performed in chloride-rich acidic media (pH 3 and 3.5 wt pct NaCl).

passive film. In addition, it is generally agreed that porosity is detrimental to the wear resistance of most steel coatings because cracks are more prone to propagate through connecting pores. With respect to the presence of crystalline phase, a high degree of crystallization significantly decreases the corrosion resistance due to phase segregation, and formation of boundaries (grains or phases) in the very homogeneous amorphous matrix. All these aspects suggest that the corrosion resistance of HVOF coatings should be superior to that of the flame-sprayed equivalents due to the microstructural features determined by thermal-spraying routes, which was confirmed in this study.

Another positive contribution to the better corrosion resistance of HVOF is related to the presence of a protective layer forming on the surface of the coating. Indeed, although not as high as in conventional stainless steels, the 8 at. pct Cr content can promote the formation of some beneficial protective oxide layer on the surface of the highly amorphous coatings. The presence of such a protective layer is consistent with the current plateau in the polarization curve and seems to be confirmed thanks to the electrochemical impedance measurements and modeling as discussed hereafter.

Table IV. Electrochemical Properties Obtained from the Polarization Curves for the HVOF and Flame-Sprayed Coatings and API 5L X80 Steel

Sample	3.5 pct NaCl Media, pH = 3		3.5 pct NaCl Media, pH = 10	
	E_{corr} (mV/SCE)	i_{corr} ($\mu\text{A}/\text{cm}^2$)	E_{corr} (mV/SCE)	i_{corr} ($\mu\text{A}/\text{cm}^2$)
HVOF coating	-420 ± 33	2.0 ± 0.5	-434 ± 17	0.4 ± 0.1
Flame-sprayed coating	-560 ± 15	34 ± 5	-431 ± 26	8 ± 2
API 5L X80 steel	-700 ± 20	40 ± 6	-703 ± 30	28 ± 8

The area of the working electrode is 1 cm^2 and the immersion time of 30 min before launch the potentiodynamic polarizations.

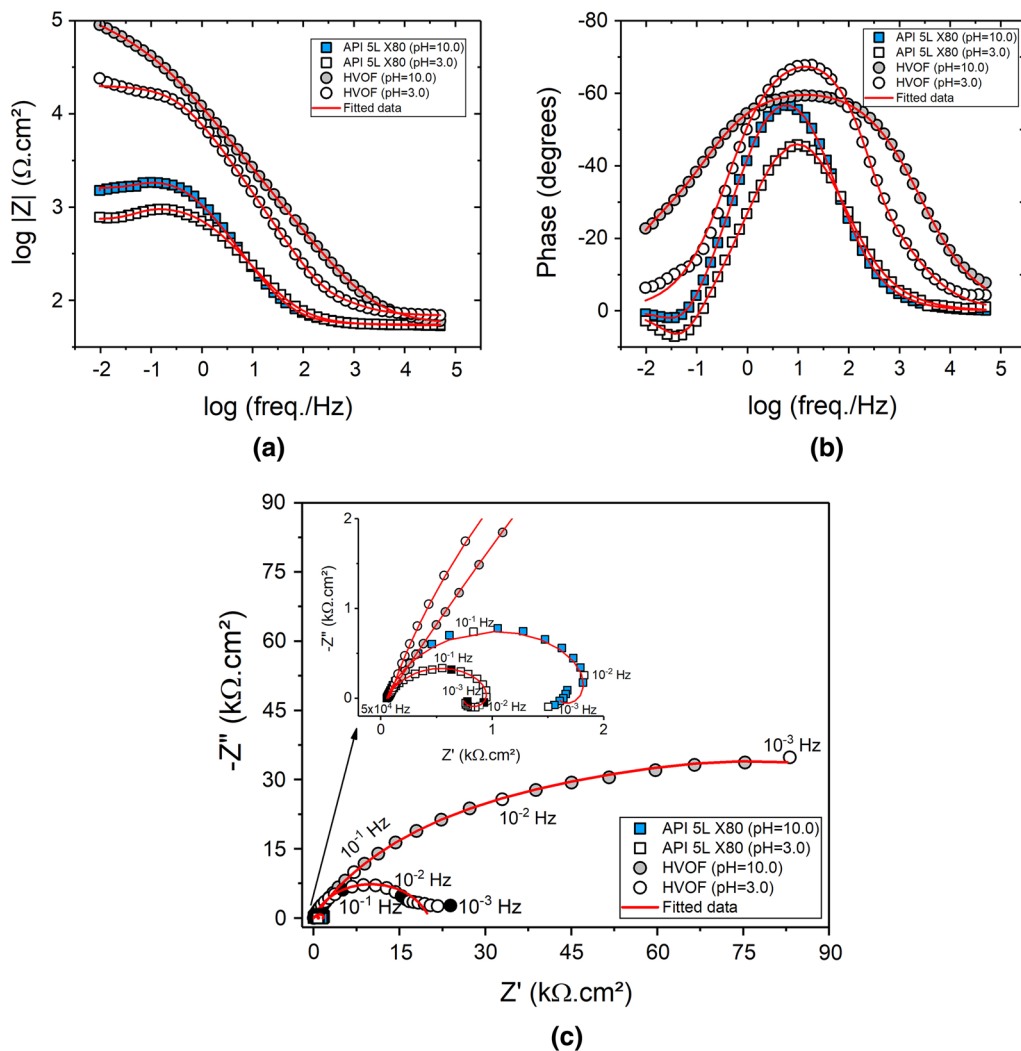


Fig. 7—Electrochemical impedance responses of HVOF coating and API 5L X80 steel in alkaline and acidic chloride-rich media (3.5 wt pct Cl). (a) Bode impedance magnitude plots, (b) Bode phase-angle plots, and (c) Nyquist diagrams. Solid lines represent the corresponding fitting results.

In order to better evaluate the protection conferred to the API 5L X80 steel by $\text{Fe}_{60}\text{Cr}_8\text{Nb}_8\text{B}_{24}$ (at. pct) HVOF coatings, EIS measurements were carried out in chloride-rich acidic and alkaline media. Figure 7 shows the Bode and Nyquist plots obtained for the different experimental conditions. In Figure 7(a), one can observe

that HVOF coatings present much higher impedance modulus ($|Z|$) than the API 5L X80 steel regardless of the media. The phase Bode and Nyquist plots (Figures 7(b) and (c), respectively) indicate that the API 5L X80 steel impedance response displays at least two-time constants, one of them related to an inductive

behavior at low frequencies. On the other hand, HVOF coatings exhibit large capacitive behavior in alkaline condition and a smaller one in acidic media, Figure 7(c).

Based on the above discussion, the EIS data, Figure 7, were simulated using two equivalent electrical circuit (EEC) models, Figure 8. For dense HVOF coatings, Figure 8(a), the EEC consists of the resistance of the solution (R_1) and a couple of in-parallel elements arranged in cascade: Q_2/R_2 (related to the protective layer formed on the surface of the dense metallic HVOF coating) and Q_3/R_3 (double-layer capacitance and reaction resistance at the electrolyte/HVOF coating interface). Constant phase element (Q) was introduced instead of a pure capacitance to consider the dispersions due to the distribution of reactivity originated from interface inhomogeneities.^[54]

Figure 8(b) shows the EEC used for API 5L X80 steel. In this case, that is, in the absence of protective film, R_1 is the resistance of the electrolyte, Q_2 is the constant phase element representing the double-layer capacitance, R_2 is the charge-transfer resistance at the metal/electrolyte interface, and R_L and L are the inductive resistance and the inductance, respectively.^[55] The inductive loop may be attributed to relaxation processes due to adsorbed species from the electrolyte, such as H_{ads}^+ and Cl_{ads}^- ,^[56,57] or to the presence on the metal surface of intermediate species formed along the dissolution mechanism.^[58] Whatever their precise origin, inductive loops are often straightforwardly related to corrosion processes,^[59,60] as it seems to be the case in this study (high i_{corr} given in Table IV) for the API steel both in acidic and alkaline media, which explicitly exhibits inductive loops in the low-frequency domain in Figures. 7(b) and (c).

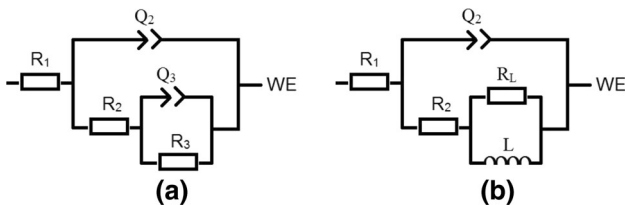


Fig. 8—Equivalent circuits used for modeling the EIS results of (a) HVOF coatings and (b) API 5L X80 steel.

Table V summarizes corrosion parameters from the fitting of equivalent circuits (Figure 7). Normalized chi-square of the data fitting ($\chi^2/|Z|$), which represents the coincidence of the fitted results with the measured data, were calculated using the software BioLogic EC-Lab V11.01. For all fitting, the $\chi^2/|Z|$ values were inferior to 10^{-3} , indicating proper fitting.

The impedance of a constant phase element is defined by $Z_Q = [Q(j)\omega]^{-\alpha}$, where the exponent α characterizes the deviation of Q from a pure capacitance. Using the constant phase element values (Q and α), R_1 , and the resistance R , the capacitance can be calculated according to Brug's equation^[61]:

$$C = \left[\frac{Q}{(R_1^{-1} + R^{-1})^{\{\alpha-1\}}} \right]^{\frac{1}{\alpha}} \quad [1]$$

Calculated values are in general in good agreement with the different models held for the HVOF coating and the mild API steel. For instance, the double-layer capacitance values of the later calculated from Eq. [1] are in good agreement with the bare metal–electrolyte interfacial double-layer capacitances (56 and 44 $\mu\text{F}/\text{cm}^2$ in basic and acidic media, respectively), as effectively expected for mild steel. Also, capacitance values obtained for protective layers assumed to be formed on the HVOF surface (2 and 44 $\mu\text{F}/\text{cm}^2$ in basic and acidic media, respectively) are within the order of magnitude of those obtained for passive films in stainless steels. This observation seems to corroborate the idea that the amorphous structure favors the formation of a more or less protective passive layer in spite of the Cr content being lower than the usual one for stainless steels.

IV. SUMMARY AND CONCLUSIONS

Mechanically milled feedstock powders of $\text{Fe}_{60}\text{Cr}_8\text{Nb}_8\text{B}_{24}$ alloy from commercial precursors were used to produce Fe-based coatings through two thermal-spraying routes: HVOF and flame spraying. Samples of both materials were characterized regarding microstructure, thermal behavior, and hardness of the

Table V. Electrochemical Parameters Calculated from EIS Data and Equivalent Circuits of HVOF Coatings and API 5L X80 Steel in Chloride-Rich (3.5 pct Cl) Acidic, pH = 3, and Alkaline, pH = 10, Media

	R_1 ($\Omega\cdot\text{cm}^2$)	Q_2 ($\mu\text{F}/\text{cm}^2$)	α_2	R_2 ($\Omega\cdot\text{cm}^2$)	Q_3 ($\mu\text{F}/\text{cm}^2$)	α_3	R_3 ($\Omega\cdot\text{cm}^2$)
HVOF pH = 10.0	56	22	0.69	49950	100	0.71	85811
HVOF pH = 3.0	69	23	0.78	150	2	1	19982
	R_1 ($\Omega\cdot\text{cm}^2$)	Q_2 ($\mu\text{F}/\text{cm}^2$)	α_2	R_2 ($\Omega\cdot\text{cm}^2$)	L (H)	R_L ($\Omega\cdot\text{cm}^2$)	
API 5L X80 pH = 10.0	55	160	0.82	1554	1040	436	
API 5L X80 pH = 3.0	54	203	0.75	690	749	303	

The area of the working electrode is 1 cm^2 and the immersion time of 30 min before launch the EIS measurements.

coatings as well as their corrosion resistances in acidic and alkaline chloride-rich media. From the above results and discussions, the following conclusions can be drawn:

- HVOF process ensured high fraction of amorphous phase with some nanocrystals embedded, high hardness ($735 \pm 25 \text{ HV}_{0.3}$), and low porosity (~ 5 pct).
- Flame-sprayed coatings exhibited a small fraction of amorphous phases in addition to $\alpha\text{-Fe}$, Fe_2B , FeNbB , and Fe_2O_3 nanocrystals; $564 \pm 15 \text{ HV}_{0.3}$, and ~ 10 pct of porosity.
- Electrochemical measurements conducted in acidic and alkaline chloride-rich media showed that HVOF coatings are more resistant to corrosion than flame-sprayed coatings due to the large fractions of amorphous phase and lower porosity, which enable the formation of a protective layer on the coating surface.
- Impedance analysis confirmed that the amorphous structure favors the formation of a more or less protective passive layer in spite of the Cr content being lower than the usual one for stainless steels.
- Highly amorphous HVOF $\text{Fe}_{60}\text{Cr}_8\text{Nb}_8\text{B}_{24}$ coatings are interesting to protect mild steel substrates commonly used in aggressive corrosion environments such as the API 5L X80 steel.

ACKNOWLEDGMENTS

This study was supported by FAPESP (thematic project, Grant Number 2013/05987-8). G.Y. Koga gratefully acknowledges the financial support of FAPESP (Grant Number 2017/09237-4). The Hydro Quebec Canada is gratefully acknowledged for its support to the production of the HVOF coatings. The authors thank Petrobras for the financial support.

REFERENCES

1. A. Inoue and X.M. Wang: *Acta Mater.*, 2000, vol. 48, pp. 1383–95.
2. Z.P. Lu, C.T. Liu, J.R. Thompson, and W.D. Porter: *Phys. Rev. Lett.*, 2004, vol. 92, pp. 1–4.
3. V. Ponnambalam, S.J. Poon, and G.J. Shiflet: *J. Mater. Res.*, 2004, vol. 19, pp. 1320–23.
4. J. Pan, Q. Chen, N. Li, and L. Liu: *J. Alloys Compd.*, 2008, vol. 463, pp. 246–49.
5. A. Inoue and A. Takeuchi: *Acta Mater.*, 2011, vol. 59, pp. 2243–67.
6. W.J. Botta, J.E. Berger, C.S. Kiminami, V. Roche, R.P. Nogueira, and C. Bolfarini: *J. Alloys Compd.*, 2014, vol. 586, pp. S105–S10.
7. M. Ashby and A. Greer: *Scr. Mater.*, 2006, vol. 54, pp. 321–26.
8. C. Suryanarayana and A. Inoue: *Int. Mater. Rev.*, 2013, vol. 58, pp. 131–66.
9. A.L. Greer, K.L. Rutherford, and I.M. Hutchings: *Int. Mater. Rev.*, 2002, vol. 47, pp. 87–112.
10. X.Q. Liu, Y.G. Zheng, X.C. Chang, W.L. Hou, and J.Q. Wang: *Mater. Sci. Forum*, 2009, vols. 633–634, pp. 685–94.
11. M.J. Duarte, S. Klemm, S. Borodin, P. Keil, K. Mayrhofer, M. Stratmann, A.H. Romero, D. Crespo, J. Serrano, P. Choi, S.S.A. Gerstl, D. Raabe, and F.U. Renner: in *Scientific Report 2009/2010*, R. Loschen and F. Stein, eds., Max-Planck-Institut für Eisenforschung GmbH, Düsseldorf, 2010, p. 192.
12. G.Y. Koga, R. Schulz, S. Savoie, A.R.C. Nascimento, Y. Drolet, C. Bolfarini, C.S. Kiminami, and W.J. Botta: *Surf. Coat. Technol.*, 2017, vol. 309, pp. 938–44.
13. R.Q. Guo, C. Zhang, Q. Chen, Y. Yang, N. Li, and L. Liu: *Corros. Sci.*, 2011, vol. 53, pp. 2351–56.
14. Z. Zhou, L. Wang, D.Y. He, F.C. Wang, and Y.B. Liu: *J. Therm. Spray Technol.*, 2010, vol. 19, pp. 1287–93.
15. C. Zhang, L. Liu, K.C. Chan, Q. Chen, and C.Y. Tang: *Intermetallics*, 2012, vol. 29, pp. 80–85.
16. H.S. Ni, X.H. Liu, X.C. Chang, W.L. Hou, W. Liu, and J.Q. Wang: *J. Alloys Compd.*, 2009, vol. 467, pp. 163–67.
17. J.M. Guilemany, J. Fernández, N. Espallargas, P.H. Suegama, and A.V. Benedetti: *Surf. Coat. Technol.*, 2006, vol. 200, pp. 3064–72.
18. J. Cheney and K. Vecchio: *Mater. Sci. Eng. A*, 2008, vol. 492, pp. 230–35.
19. Y. Guo, G.Y. Koga, A. Moreira Jorge, Jr., S. Savoie, R. Schulz, C. Kiminami, C. Bolfarini, and W.J. Botta: *Mater. Des.*, 2016, vol. 111, pp. 608–15.
20. G.Y. Koga, R.P. Nogueira, V. Roche, A.R. Yavari, A.K. Melle, J. Gallego, C. Bolfarini, C.S. Kiminami, and W.J. Botta: *Surf. Coat. Technol.*, 2014, vol. 254, pp. 238–43.
21. J.B. Cheng, Z.H. Wang, and B.S. Xu: *J. Therm. Spray Technol.*, 2012, vol. 21, pp. 1025–31.
22. S. Alleg, M. Ibrir, N.E. Fenineche, R. Bensalem, and J.J. Suñol: *Surf. Coat. Technol.*, 2010, vol. 205, pp. 281–86.
23. Y. Wu, P. Lin, Z. Wang, and G. Li: *J. Alloys Compd.*, 2009, vol. 481, pp. 719–24.
24. D. Zois, A. Lekatou, M. Vardavoulias, and A. Vazdirvanidis: *J. Alloys Compd.*, 2010, vol. 495, pp. 611–16.
25. G. Liu, Y. An, Z. Guo, J. Chen, G. Hou, and J. Chen: *Appl. Surf. Sci.*, 2012, vol. 258, pp. 5380–86.
26. J. Cheng, X. Liang, B. Xu, and Y. Wu: *J. Non-cryst. Solids*, 2009, vol. 355, pp. 1673–78.
27. W. Guo, J. Zhang, Y. Wu, S. Hong, and Y. Qin: *Mater. Des.*, 2015, vol. 78, pp. 118–24.
28. C. Zhang, R.Q. Guo, Y. Yang, Y. Wu, and L. Liu: *Electrochim. Acta*, 2011, vol. 56, pp. 6380–88.
29. Y. Wu, P. Lin, G. Xie, J. Hu, and M. Cao: *Mater. Sci. Eng. A*, 2006, vol. 430, pp. 34–39.
30. H.W. Jin, Y.M. Rhyim, S.G. Hong, and C.G. Park: *Mater. Sci.*, 2001, vol. 306, pp. 1069–74.
31. J. Voyer: *J. Therm. Spray Technol.*, 2010, vol. 19, pp. 1013–23.
32. B. Uyulgan, E. Dokumaci, E. Celik, I. Kayatekin, N.F. Ak Azem, I. Ozdemir, and M. Toparli: *J. Mater. Process. Technol.*, 2007, vol. 190, pp. 204–10.
33. S.D. Zhang, J. Wu, W.B. Qi, and J.Q. Wang: *Corros. Sci.*, 2016, vol. 110, pp. 57–70.
34. Y. Huang, Y. Guo, H. Fan, and J. Shen: *Mater. Lett.*, 2012, vol. 89, pp. 251–53.
35. Z. Zhou, L. Wang, F.C. Wang, H.F. Zhang, Y.B. Liu, and S.H. Xu: *Surf. Coat. Technol.*, 2009, vol. 204, pp. 563–70.
36. C. Suryanarayana: *Prog. Mater. Sci.*, 2001, vol. 46, pp. 1–184.
37. J.C. Farmer, J.J. Haslam, S.D. Day, T. Lian, C.K. Saw, P.D. Hailey, J.-S. Choi, R.B. Rebak, N. Yang, J.H. Payer, J.H. Perepezko, K. Hildal, E.J. Lavernia, L. Ajdelsztajn, D.J. Branagan, E.J. Buffa, and L.F. Aprigliano: *J. Mater. Res.*, 2007, vol. 22, pp. 2297–2311.
38. S.J. Pang, T. Zhang, K. Asami, and A. Inoue: *Acta Mater.*, 2002, vol. 50, pp. 489–97.
39. V. Ponnambalam, S.J. Poon, and G.J. Shiflet: *J. Mater. Res.*, 2004, vol. 19, pp. 3046–52.
40. S. Sharma and C. Suryanarayana: *J. Appl. Phys.*, 2008, vol. 103, p. 13504.
41. X.J. Gu, S.J. Poon, and G.J. Shiflet: *Scr. Mater.*, 2007, vol. 57, pp. 289–92.
42. J. Balogh, T. Kemeny, I. Vincze, L. Bujdosó, L. Toth, and G. Vincze: *J. Appl. Phys.*, 1995, vol. 77, pp. 4997–5003.
43. N. Al-Aqeeli, M.A. Hussein, and C. Suryanarayana: *Adv. Powder Technol.*, 2015, vol. 26, pp. 385–91.
44. F.Q. Guo and K. Lu: *Metall. Mater. Trans. A*, 1997, vol. 28, pp. 1123–31.

45. K. Lu and J.T. Wang: *Mater. Sci. Eng. A*, 1991, vol. 133, pp. 500–03.
46. B. Yao, S.E. Liu, L. Liu, L. Si, W.H. Su, and Y. Li: *J. Appl. Phys.*, 2001, vol. 90, pp. 1650–54.
47. W. Yuping, L. Pinghua, C. Chenglin, W. Zehua, C. Ming, and H. Junhua: *Mater. Lett.*, 2007, vol. 61, pp. 1867–72.
48. H. Miura, S. Isa, K. Omuro, and N. Tanigami: *Trans. Japan Inst. Met.*, 1981, vol. 22, pp. 597–606.
49. Y. Wang, S.L. Jiang, Y.G. Zheng, W. Ke, W.H. Sun, and J.Q. Wang: *Surf. Coat. Technol.*, 2011, vol. 206, pp. 1307–18.
50. S.D. Zhang, W.L. Zhang, S.G. Wang, X.J. Gu, and J.Q. Wang: *Corros. Sci.*, 2015, vol. 93, pp. 211–21.
51. M.J. Duarte, J. Klemm, S.O. Klemm, K.J.J. Mayrhofer, M. Stratmann, S. Borodin, A.H. Romero, M. Madinehei, D. Crespo, J. Serrano, S.S. Gerstl, P.P. Choi, D. Raabe, and F.U. Renner: *Science*, 2013, vol. 341, pp. 372–76.
52. C.A.C. Souza, M.F. de Oliveira, J.E. May, W.J. Botta, N.A. Mariano, S.E. Kuri, and C.S. Kiminami: *J. Non-cryst. Solids*, 2000, vol. 273, pp. 282–88.
53. C.A.C. Souza, D.V. Ribeiro, and C.S. Kiminami: *J. Non-cryst. Solids*, 2016, vol. 442, pp. 56–66.
54. P. Córdoba-Torres, T.J. Mesquita, and R.P. Nogueira: *Electrochim. Acta*, 2013, vol. 92, pp. 323–34.
55. H.H. Hassan, E. Abdelghani, and M.A. Amin: *Electrochim. Acta*, 2007, vol. 52, pp. 6359–66.
56. H.J.W. Lenderink, M.V.D. Linden, and J.H.W. Wit: *Electrochim. Acta*, 1993, vol. 38, pp. 1989–92.
57. M.A. Veloz and I. Gonzalez: *Electrochim. Acta*, 2002, vol. 48, pp. 135–44.
58. F. Farelàs, M. Galicia, B. Brown, S. Nestic, and H. Castaneda: *Corros. Sci.*, 2010, vol. 52, pp. 509–17.
59. P. Córdoba-Torres, M. Keddad, and R.P. Nogueira: *Electrochim. Acta*, 2008, vol. 54, pp. 518–23.
60. B. Huet, R.P. Nogueira, and H. Takenouti: in *ASM Handbook*, A.S.M. Handbook, D. Cramer, and B.S. Covino, Jr, eds., ASM International, Materials Park, 2003, pp. 52–60.
61. G.J. Brug, A.L.G. van den Eeden, M. Sluyters-Rehbach, and J.H. Sluyters: *J. Electroanal. Chem. Interfacial Electrochem.*, 1984, vol. 176, pp. 275–95.